REVIEW

Recent developments of the reconstruction in magnetic particle imaging

Lin Yin[1,2,3†] , Wei Li[4†], Yang Du[1,2,3], Kun Wang[1,2,3], Zhenyu Liu[1,2,3], Hui Hui[1,2,3*] and Jie Tian[1,2,3,5*]

Abstract

Magnetic particle imaging (MPI) is an emerging molecular imaging technique with high sensitivity and temporal-spatial resolution. Image reconstruction is an important research topic in MPI, which converts an induced voltage signal into the image of superparamagnetic iron oxide particles concentration distribution. MPI reconstruction primarily involves system matrix- and x-space-based methods. In this review, we provide a detailed overview of the research status and future research trends of these two methods. In addition, we review the application of deep learning methods in MPI reconstruction and the current open sources of MPI. Finally, research opinions on MPI reconstruction are presented. We hope this review promotes the use of MPI in clinical applications.

Keywords: Magnetic particle imaging, Image reconstruction, System matrix, X-space

Introduction

Magnetic particle imaging (MPI) is a novel molecular imaging modality that can image superparamagnetic iron oxide particles (SPIOs) with high temporal-spatial resolution and sensitivity in a noninvasive manner [1–4]. In 2005, Gleich and Weizenecker [1] first proposed the physical principles and wide application prospects of MPI. The imaging principle of MPI is related to the nonlinear magnetization response of SPIOs in a magnetic field. First, a gradient field generated by a permanent magnet or energized coil is used to create a field-free region (FFR). Subsequently, by superimposing an oscillating drive field, the FFR moves through the field of view (FOV) [5, 6]. The excitation field influences SPIOs near the FFR to undergo a nonlinear magnetization response to generate a voltage signal in the receiving coils (Fig. 1 A). When SPIOs enter the magnetic-field saturation region, SPIOs are not magnetized to produce voltage signals (Fig. 1 B). The concentration distribution of the SPIOs can be further obtained by analyzing the reconstruction algorithm from the signal to the image [7, 8].
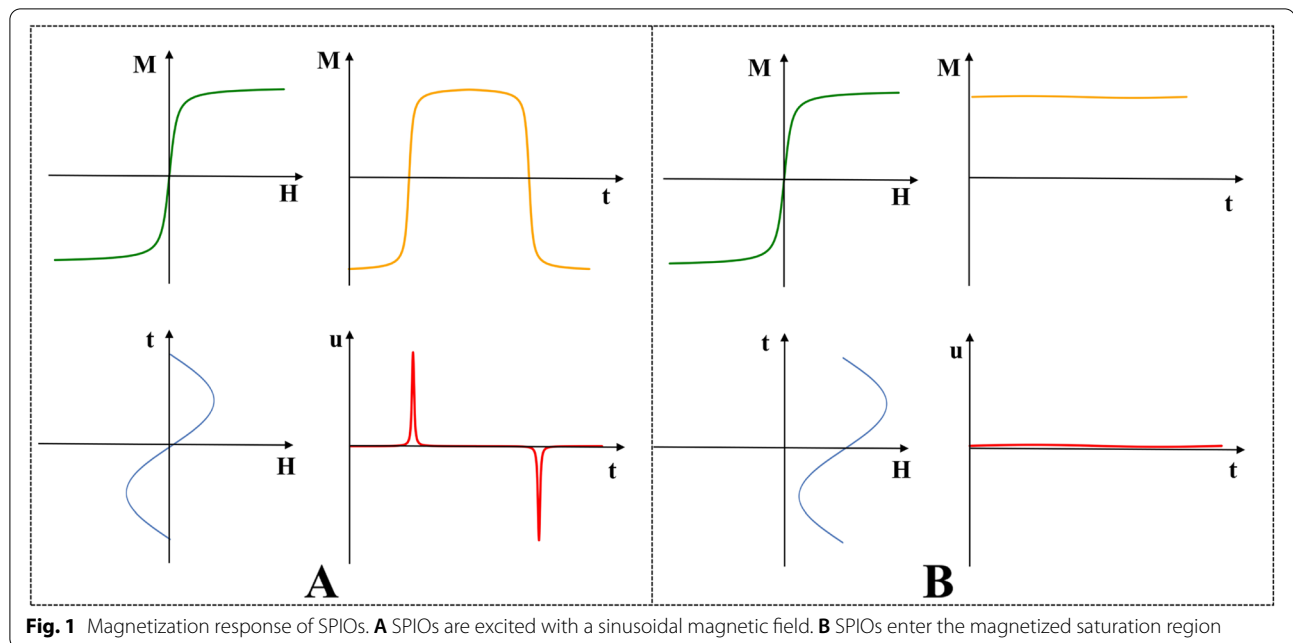
Compared with current powerful imaging techniques, MPI has significant advantages. Computed tomography (CT) and magnetic resonance imaging (MRI) can achieve a sub-millimeter spatial resolution, but their sensitivity is limited, resulting in poor specificity at the molecular level [4]. Positron emission tomography (PET) and single-photon emission computed tomography (SPECT) have high sensitivity but a spatial resolution of approximately 3 mm. In addition, these applications are limited by the short half-life of radioactive tracers in cell tracking or other several research fields that require long observations [9]. Optical imaging technology can achieve a high sensitivity and spatial-resolution imaging, but its imaging depth is limited to 2-3 cm [10, 11]. MPI is expected to overcome the limitations of molecular imaging technology in terms of imaging depth, sensitivity, resolution, and radiation, thereby becoming a new trend in the development of high-end medical imaging that represents the international academic frontier of the development of modern medical imaging [4, 12–14]. Table 1 presents quantitative comparisons between different imaging modalities.

[†]Lin Yin and Wei Li contributed equally to this work.

*Correspondence: hui.hui@ia.ac.cn; tian@ieee.org

[3] University of Chinese Academy of Sciences, Beijing 100049, China
[5] Beijing Advanced Innovation Center for Big Data-Based Precision Medicine, School of Medicine, Beihang University, Beijing 100083, China
Full list of author information is available at the end of the article

Yin *et al. Visual Computing for Industry, Biomedicine, and Art*   (2022) 5:24

Page 2 of 13

Fig. 1 Magnetization response of SPIOs. **A** SPIOs are excited with a sinusoidal magnetic field. **B** SPIOs enter the magnetized saturation region

As a new molecular imaging technology, MPI plays an increasingly important role in many preclinical biomedical studies. MPI has been proven to achieve a highly sensitive detection of approximately 250 cells in vivo in cell tracking studies [15]. MPI has provided the highest imaging sensitivity in multimodality dynamic observations of gliomas [16, 17]. MPI can also detect and visualize the homing of breast tumor cells with high sensitivity [18]. MPI has also been successfully applied in cardiovascular and cerebrovascular imaging [19, 20] and neuroimaging [21]. These advances fully demonstrate the imaging advantages of the high sensitivity and specificity of MPI, demonstrating the great potential and value of this new molecular imaging technology.

In recent years, the imaging theory and instruments for MPI have been continuously improved and developed. In 2008, instead of moving the object mechanically in a horizontal direction, Gleich et al. [22] achieved fast two-dimensional (2D) imaging by superposing a horizontal drive field. In the same year, they proposed a field-free line (FFL), which is an effective encoding scheme for MPI. The results of the simulations demonstrated an obvious improvement in image quality compared with the existing field-free point (FFP) [23–26]. Subsequently, novel single-sided MPI equipment was proposed by Sattel et al. [27], which overcame the limitations of specimen size. In 2009, they achieved the first three-dimensional (3D) real-time in vivo MPI [2]. In 2013, the world's first commercial MPI scanner (based on FFP) was released by Bruker Biospin. In 2014, the Magnetic Insight company from the United States unveiled the world's second commercial MPI scanner (based on FFL) [4]. In 2015, a superspeed traveling wave MPI scanner was proposed to realize superspeed imaging of magnetic particle flows [28]. In 2016, Franke et al. [29] designed a hybrid system that combined MRI and MPI. In 2019, Gräser et al. [30] designed an MPI scanner with the size of the human brain. In 2020, scientists from Turkey proposed an open-sided MPI scanner system based on the FFL scheme [31]. In 2021, a novel handheld MPI scanner was designed for the intraoperative imaging of breast nodules [32]. Figure 2 shows the development timeline of MPI.

With the continuous development of MPI scanners, abundant research on MPI reconstruction has been conducted to enhance the imaging performance of the instruments. MPI reconstruction algorithms are primarily of two types of methods: system matrix (SM) and x-space. SM-based MPI reconstruction is an important field [33–35]. The acquisition of SMs in SM-based MPI reconstructions is an important research topic. Currently, three methods have been reported for obtaining SMs: measurement-based SM, sparse recovery SM, and model-based SM. Owing to the complex magnetic environment and magnetization behavior of SPIOs, the development of an accurate physical model remains a challenging problem. Therefore, the first reported, and the most accurate method, is measurement-based SM acquisition, which involves moving a delta sample with a robot at all positions of the entire FOV [1, 36]. Despite its high accuracy, the measurement process is time consuming. In addition, the measured SM requires a lot of memory, which leads to inefficient reconstruction. Therefore,

Table 1 Quantitative comparisons of different imaging modalities

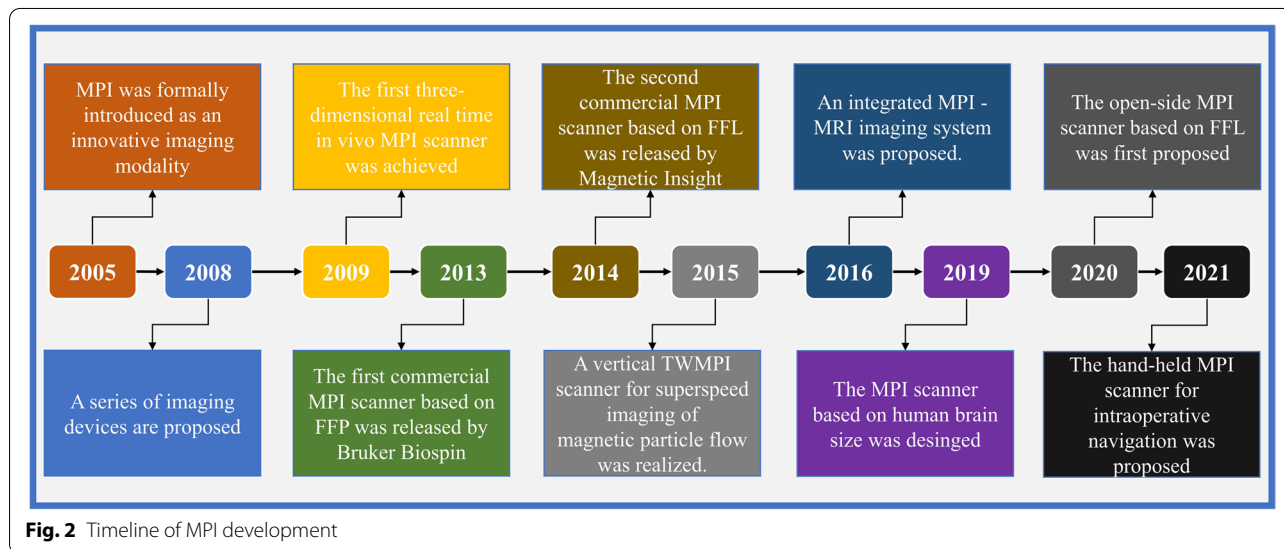| Property	CT	MRI	PET/SPECT	Optical imaging	MPI
Spatial resolution	< 1 mm	< 1 mm	3 mm	< 1 mm	< 1 mm
Temporal resolution	1 s	1 s-1 h	1 min	< 0.1 s	< 0.1 s
Sensitivity	Low	Low	High	High	High
Depth	High	High	High	2-3 cm	High
Radioactivity	Yes	No	Yes	No	No

Fig. 2 Timeline of MPI development

sparse recovery methods and model-based SM acquisition have been proposed [37, 38]. In addition to the SM acquisition method, a reconstruction strategy based on SM is an important research topic. Further details regarding this are covered later in this review.

X-space methods are another important component of MPI reconstruction [39–42]. This study reviews the basic theory and improved algorithms developed in recent years. In addition, with the current development of artificial intelligence (AI), strategies based on deep learning networks have also shined in the field of MPI reconstruction. We review the relevant research in detail. Furthermore, there is an increasing number of MPI research groups around the world, as well as many open-source data, programs, and software platforms, which are also discussed in this review. Finally, the conclusions and outlook of MPI are presented.

SM-based MPI reconstruction

The objective of MPI reconstruction is to transform the induced voltage signal into a spatial concentration distribution of the SPIOs. A SM is a mapping of the two items, considering the complex magnetic field and SPIOs properties [7, 36, 43]. The linear mapping between the induced voltage signal u_k (Fourier coefficients of the time-domain signal $u(t)$) and SPIO concentration $c(\mathbf{r})$ can be described as follows:

$$u_k = \int_\Omega s_k(\mathbf{r})c(\mathbf{r})d^3\mathbf{r}, \ \ k = 1,\ldots,K \qquad (1)$$

where $\mathbf{r}$ represents the spatial position, and $s_k(\mathbf{r})$ denotes the system function. K denotes the total number of frequency components. By sampling all N positions of the FOV, we obtain the following linear relationship:

$$\mathbf{u} = \mathbf{Sc} \qquad (2)$$

where $\mathbf{S} \in \mathbb{C}^{K \times N}$ denotes the SM. $\mathbf{u} \in \mathbb{C}^{K \times 1}$ and $\mathbf{c} \in \mathbb{R}^{N \times 1}$ denote the voltage and SPIOs concentration vector, respectively.

SM-based reconstruction plays an important role in MPI reconstruction. This section describes the commonly used SM acquisition methods and reconstruction strategies based on SM.
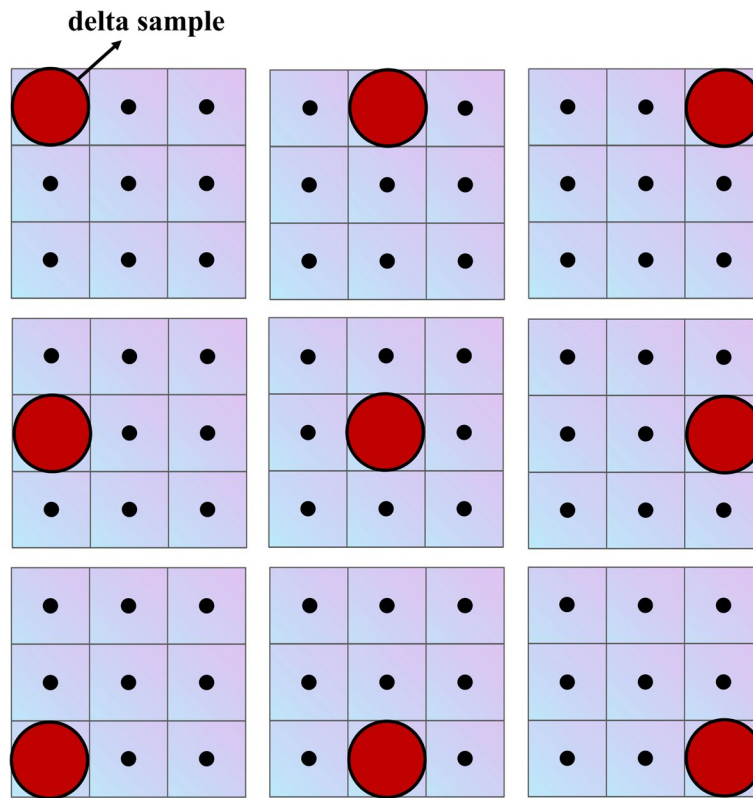
Yin *et al. Visual Computing for Industry, Biomedicine, and Art* (2022) 5:24

Page 4 of 13

Fig. 3 Principle of measurement-based SM method of MPI using a delta sample (taking a grid of 3×3 as an example). A robot moves the delta sample to scan the location of each pixel

Acquiring the SM

Measurement-based methods

A tedious calibration procedure must be performed for the measurement-based SM acquisition method. Figure 3 shows the calibration procedure for the measurement-based method. It measures the induced voltage signal at all positions in the FOV with a delta sample to obtain the SM. Even a medium-sized image of 34×28×20 can require up to six hours to measure the SM [2, 37]. Therefore, a high-quality image requires a time-consuming and tedious calibration procedure. In addition, when the experimental conditions change, such as changes in particle species and magnetic field intensity, the SM must be recalibrated. In addition, cooling is required during calibration because the coils overheat after prolonged system operation [44].

Sparse recovery methods Owing to the complexity and time requirements of the measurement-based SM acquisition method, many studies have proposed sparse recovery methods to obtain a complete SM using only a subset of all calibration scans. In 2013, Knopp and Weber [37] proposed using the sparsity of SMs based on certain basis transformations (such as the discrete Fourier transform,

discrete cosine transform or discrete Chebyshev transform) for compressed sensing (CS) reconstruction to significantly reduce the number of calibration scans. Each row of the SM is handled separately. Taking the k-th row as an example, an inverse problem must be solved:

$$\arg\min_{\mathbf{x}} \ \|\Phi\mathbf{x}\|_1 \quad \text{subj.to } \frac{1}{2}\|\mathbf{P}\mathbf{x} - \mathbf{y}_k\|_2^2 < \varepsilon^2 \qquad (3)$$

where $\Phi \in \mathbb{C}^{N \times N}$ denotes a basis transformation matrix, $\mathbf{x} \in \mathbb{C}^{N \times 1}$ denotes the optimization results, and $\mathbf{P}$ represents the undersampled matrix, which denotes the position index of the points sampled from the k-th row $\mathbf{s}_k$. $\mathbf{y}_k$ denotes the undersampled measurement: $\mathbf{y}_k = \mathbf{P}\mathbf{s}_k$. Several algorithms have been proposed to solve this inverse problem [37]. The sparse recovery method based on the standard CS can reduce the sampling rate by 10% [37].

Based on CS theory, many improved sparse recovery algorithms have also been extended. Weber and Knopp [45] proposed the use of SM symmetry to further compress SMs (Fig. 4). Grosser et al. [44] proposed the use of low-rank tensors to represent SMs, which allows SM recovery even when the sampling rate is reduced to 2%. Ilbey et al. [46] presented a framework for a coded calibration scene. Compared with the standard CS
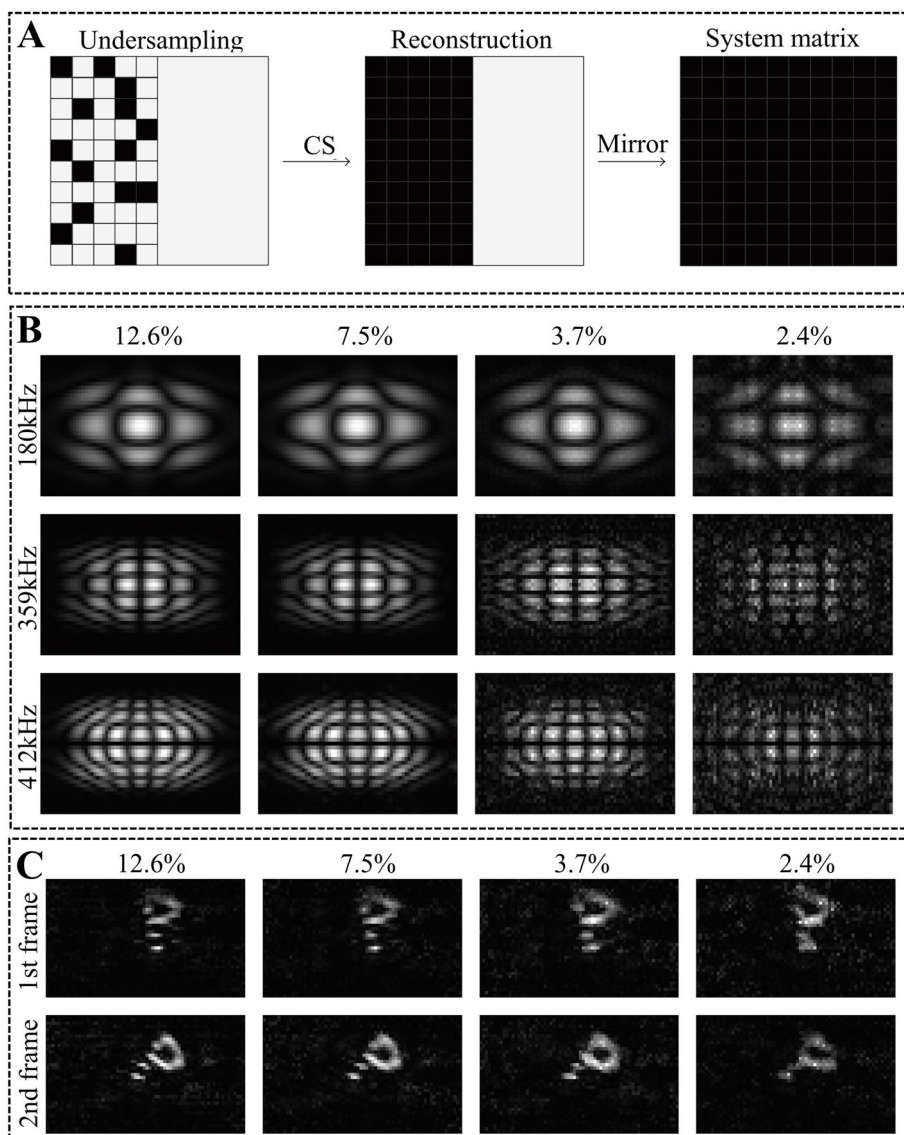
Yin *et al. Visual Computing for Industry, Biomedicine, and Art*   (2022) 5:24

Page 5 of 13

Fig. 4 A The principle of the CS-symmetry method: the first half of the SM is recovered based on the CS method. Then, the complete SM is recovered based on mirror symmetry (alternatively, by changing the order of the two steps, symmetry-CS is permissible). **B** The SM components at different frequencies recovered with the symmetry-CS method at different sampling rates. **C** Reconstructed phantom results of the recovered SM at different sampling rates based on the symmetry-CS method. For more images see ref. [45]

method, the image quality is significantly improved under the same signal-noise ratio (SNR) and sampling rate [46]. Sparse recovery algorithms can significantly reduce the calibration time and guarantee the quality of image reconstruction, which has attracted increasing attention in the field of MPI reconstruction.

Model-based methods   In addition to the measurement-based and sparse recovery methods, Knopp et al. [38] proposed a model-based method in 2010. They used the model of a signal chain to generate SMs. This approach consisted of three steps.

1) Signal encoding: the principle of the signal chain is used to model signal encoding. In MPI, the relationship between the time-domain induced voltage $u(t)$ in the receiving coil and SPIO concentration $c(\mathbf{r})$ is as follows:

$$u(t) = -\mu_0 \int_\Omega \frac{\partial}{\partial t} \mathbf{M}(\mathbf{r}, t) \cdot \mathbf{p}(\mathbf{r}) c(\mathbf{r}) d\mathbf{r} \tag{4}$$

where μ_0 represents the permeability of a vacuum, and $\mathbf{M}(\mathbf{r}, t)$ denotes the unit magnetization of the SPIOs. $\mathbf{p}(\mathbf{r})$

is the sensitivity profile of the recording coil. Because filtering is easier in the frequency domain, processing is generally performed in the frequency domain to increase the accuracy of the modeled-induced voltage:

$$u_k = \int_\Omega \left(a_k \int_0^T \frac{\partial}{\partial t} \mathbf{M}(\mathbf{r}, t) \cdot \mathbf{p}(\mathbf{r}) e^{2\pi i k t/T} dt \right) c(\mathbf{r}) d\mathbf{r} \tag{5}$$

where a_k is the transfer function. Comparing Eqs. (1), (4), and (5), the model-based system function is obtained as follows:

$$s_k^{model}(\mathbf{r}) = a_k \int_0^T \frac{\partial}{\partial t} \mathbf{M}(\mathbf{r}, t) \cdot \mathbf{p}(\mathbf{r}) e^{2\pi i k t/T} dt \tag{6}$$

2) Particle model: Langevin is the most commonly used model for describing the magnetization of SPIOs:

$$\mathbf{M}(\mathbf{r}, t) = \mathbf{e_H} \int_0^\infty \rho(D) m \left(coth(\xi) - \frac{1}{\xi} \right) dD \tag{7}$$

with

$$\xi = \frac{\mu_0 m \|\mathbf{H}(\mathbf{r}, t)\|_2}{k_B T} \tag{8}$$

where K_B and T are the Boltzmann constant and temperature, respectively. m denotes the magnetic moment, and $\mathbf{e_H} = \mathbf{H}(\mathbf{r}, t)/\|\mathbf{H}(\mathbf{r}, t)\|_2$ denotes the direction of the magnetic field strength. D represents the diameters of the SPIOs.

3) Transfer function: a_k can be obtained by minimizing the following equation:

$$f(a_k) = \int_\Omega |s_k^{meas}(\mathbf{r}) - a_k \hat{s}_k^{model}(\mathbf{r})|^2 d\mathbf{r} \tag{9}$$

where k denotes the frequency index, s_k^{meas} denotes the measured system function, and $\hat{s}_k^{model} = s_k^{model}/a_k$. a_k can be computed as follows.

$$a_k = \frac{\int_\Omega s_k^{meas}(\mathbf{r}) \overline{\hat{s}_k^{model}(\mathbf{r})} d\mathbf{r}}{\int_\Omega |\hat{s}_k^{model}(\mathbf{r})|^2 d\mathbf{r}} \tag{10}$$

In principle, a measured system function with a single position is sufficient for obtaining a_k. This approach demonstrates the feasibility of modeling instead of measuring SMs [38]. Subsequently, Knopp et al. [47] verified the accuracy of a model-based SM acquisition method on 2D data. Model-based SM acquisition methods can accurately model the system function based on a few calibration scans, and the accuracy can be increased by improving the underlying physical model.

SM-based MPI reconstruction based on the regularization strategy

After obtaining the SM, the concentration distribution of the SPIOs can be obtained by solving Eq. (2) using a series of optimization algorithms. Owing to the ill-posedness of the inverse problem, a regularization strategy was introduced to improve the accuracy of image reconstruction. Tikhonov regularization is the most commonly used method and is widely used in MPI reconstruction owing to its fast and simple implementation [3]:

$$\arg \min_{\mathbf{c} \geq 0} \|\mathbf{W}^{1/2}(\mathbf{Sc} - \mathbf{u})\|_2^2 + \lambda \|\mathbf{c}\|_2^2 \tag{11}$$

where λ denotes the regularization parameter that penalizes the solution with a large Euclidean norm. $\mathbf{W}$ denotes the weighting matrix used to normalize the elements of the SM.

Both direct and iterative methods are used to solve the Tikhonov regularization. Examples of direct methods are Cholesky decomposition or singular value decomposition (SVD) [48, 49]. Direct methods have several advantages. For example, SVD can flexibly tune the regularization parameters with only a small amount of computational effort. However, the complete SM must typically be stored in memory while solving Eq. (11), which is unfeasible for a huge SM of 3D MPI.

Therefore, iterative methods have emerged with a high demand in MPI, leading to less memory and computational effort in several cases. Popular iterative methods include the conjugate gradient method [48] and Kaczmarz method [50, 51]. The Kaczmarz method is a row-action method that operates on rows independently. Convergence has been reported to occur within ten iterations of the Kaczmarz method [52]. Therefore, the state-of-the-art method for SM-based reconstruction is the Tikhonov regularization solved by the Kaczmarz method [53]. In recent years, many Kaczmarz-related Tikhonov regularization solutions have emerged in the field of MPI reconstruction [3, 50, 54].

Although Tikhonov regularization is simple and easy to implement, it does not use the inherent spatial neighborhood structure priori to improve the image quality. Therefore, to introduce the neighborhood structure, Storath et al. [55] proposed nonnegative fused LASSO regularization and achieved edge-preserving and noise-reducing reconstruction for MPI. The form of the fused LASSO regularization is as follows:

$$\arg \min_{\mathbf{c} \geq 0} \frac{1}{2} \|\mathbf{Sc} - \mathbf{u}\|_2^2 + \alpha TV(\mathbf{c}) + \beta \|\mathbf{c}\|_1 \tag{12}$$

where $TV(\mathbf{c})$ denotes the total variation that promotes a sparse edge. $\|\mathbf{c}\|_1$ represents the L_1 norm. α and β are

regularization parameters. Storath et al. [55] also introduced nonnegativity to model a (12) and defined it as nonnegative fused LASSO regularization. Compared with Tikhonov regularization, nonnegative fused LASSO regularization is more robust to Gaussian noise. In addition, the reconstructed images showed sharp boundaries and uniformity. Regularization technology plays an important role in the field of SM-based MPI reconstruction and is an important approach to further improve image quality.

X-space methods for MPI reconstruction

X-space methods are another important research topic for MPI reconstruction [39]. X-space and SM-based reconstruction differ significantly. Specifically, x-space can achieve a real-time reconstruction by dividing the velocity of the FFR based on the linear shift-invariant (LSI) system.

Mathematically, the theory of one-dimensional (1D) x-space in MPI can be described as follows:

$$u(t) = \mathbf{p}(\mathbf{r})G\dot{\mathbf{r}}_s(t)c(\mathbf{r}) * h(\mathbf{r}) \tag{13}$$

where $\dot{\mathbf{r}}_s(t)$ denotes the velocity of the FFR (In this review, we consider FFP as an example.). $\mathbf{p}(\mathbf{r})$ is the sensitivity of the receiver coil, and G denotes the gradient strength. $h(r) = \frac{d\mathbf{M}}{d\mathbf{H}}$ represents the point spread function (PSF), which is the derivative of the Langevin function:

$$h(\mathbf{r}) = m\dot{\mathcal{L}}(\xi\mathbf{H}) \tag{14}$$

The raw MPI image was obtained using a simple two-step velocity-compensation process. MPI reconstruction is performed by gridding the induced voltage signal to the velocity of the FFP:

$$\hat{c}(\mathbf{r}) = c(\mathbf{r}) * h(\mathbf{r}) = \frac{u(t)}{\mathbf{p}(\mathbf{r})G\dot{\mathbf{r}}_s(t)} \tag{15}$$

where $\hat{c}(\mathbf{r})$ denotes the raw MPI image, which can be described as the convolution of the real MPI image $c(\mathbf{r})$ with a PSF.

The MPI voltage signal can be regarded as a sampling operation in the raw MPI image $\hat{c}(\mathbf{r})$ at the instantaneous position of the FFP. Therefore, $\hat{c}(\mathbf{r})$ can be reconstructed by the velocity compensation and meshing of the MPI voltage signal based on the position of the FFP.

In 2011, Goodwill and Conolly [56] extended 1D x-space theory to 2D and 3D x-space reconstruction. They proved that 3D MPI is also an LSI imaging process and derived the 3D PSF of MPI. Furthermore, they verified the feasibility of the 3D x-space method on a theoretical basis and conducted 2D MPI verification based on an x-space MPI scanner. However, the quality

of reconstructed images must be improved. A year later, Goodwill et al. [57] proposed the projection x-space MPI theory based on FFL scanning. They used permanent magnets to generate the FFL for the first time and provided the first FFL-based MPI images. Fast 3D MPI scans were performed using a FFL-based projection x-space to further improve image quality and sharpness. However, classical x-space methods ignore the relaxation effects of SPIOs and assume SPIOs are instantaneously magnetized with the magnetic field, possibly diminishing the MPI signal and causing artifacts in the reconstructed images [58, 59].

X-space methods based on relaxation models

Classical x-space methods use the Langevin model under the adiabatic hypothesis to describe the magnetization process of SPIOs:

$$\mathbf{M}_L(\mathbf{r}, t) = m\mathcal{L}(\xi\mathbf{H}) \tag{16}$$

However, in practice, SPIOs cannot operate in an ideal adiabatic environment. In a nonadiabatic environment, SPIOs change with the magnetization delay, which is often referred to as relaxation effects or relaxation time. Therefore, errors occur when using the Langevin model to describe the magnetization process of SPIOs under adiabatic assumptions, leading to blurred and inaccurate x-space reconstructed images (Fig. 5 A).

Several research groups have proposed improved x-space methods based on relaxation models to account for the relaxation effects and accurately describe the magnetization process. Croft et al. [60] theoretically and experimentally demonstrated the blurring of x-space images and deterioration of resolution and SNR caused by relaxation effects. Furthermore, they proposed a simple relaxation model called the Debye model to achieve a desirable signal strength and resolution (Fig. 5 B). A differential equation in the Debye model is as follows:

$$\frac{d\mathbf{M}_D(\mathbf{r}, t)}{dt} = -\frac{\mathbf{M}_D(\mathbf{r}, t) - \mathbf{M}_L(\mathbf{r}, t)}{\tau} \tag{17}$$

where $\mathbf{M}_D(\mathbf{r}, t)$ denotes the Debye model that describes nonadiabatic magnetization. τ denotes the relaxation-time constant. Furthermore, by solving this differential equation, the following temporal convolution formulation can be obtained:

$$\mathbf{M}_D(\mathbf{r}, t) = \mathbf{M}_L(\mathbf{r}, t) * \frac{1}{\tau}\exp(-t/\tau)p(t) = \mathbf{M}_L(\mathbf{r}, t) * q(t) \tag{18}$$

where $p(t)$ denotes the Heaviside function, with $\tau > 0$. Nonadiabatic magnetization can be described as the temporal convolution of the adiabatic magnetization and
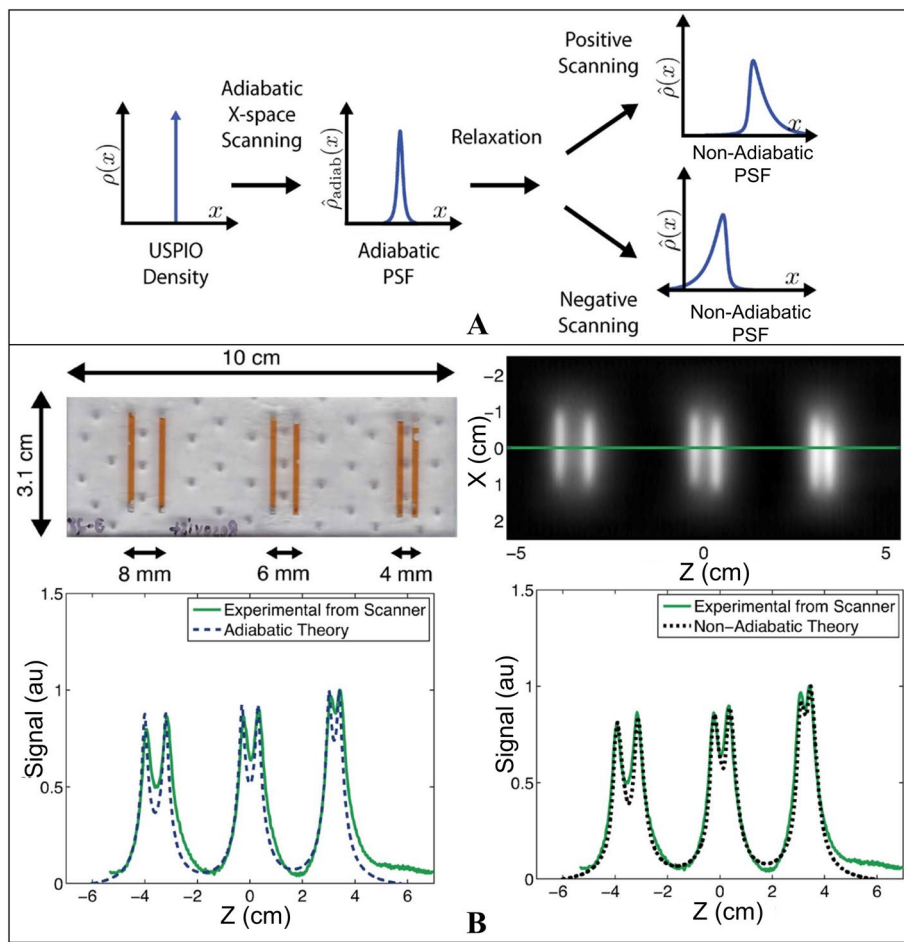
Yin *et al. Visual Computing for Industry, Biomedicine, and Art*   (2022) 5:24

Page 8 of 13

Fig. 5 **A** Comparison between adiabatic and nonadiabatic x-space scanning. The blurs caused by the relaxation effects occur in two scanning directions, which lead to nonidentical PSFs. **B** Experiments and reconstructed results of line phantoms with different spacing. For more images see ref. [60]
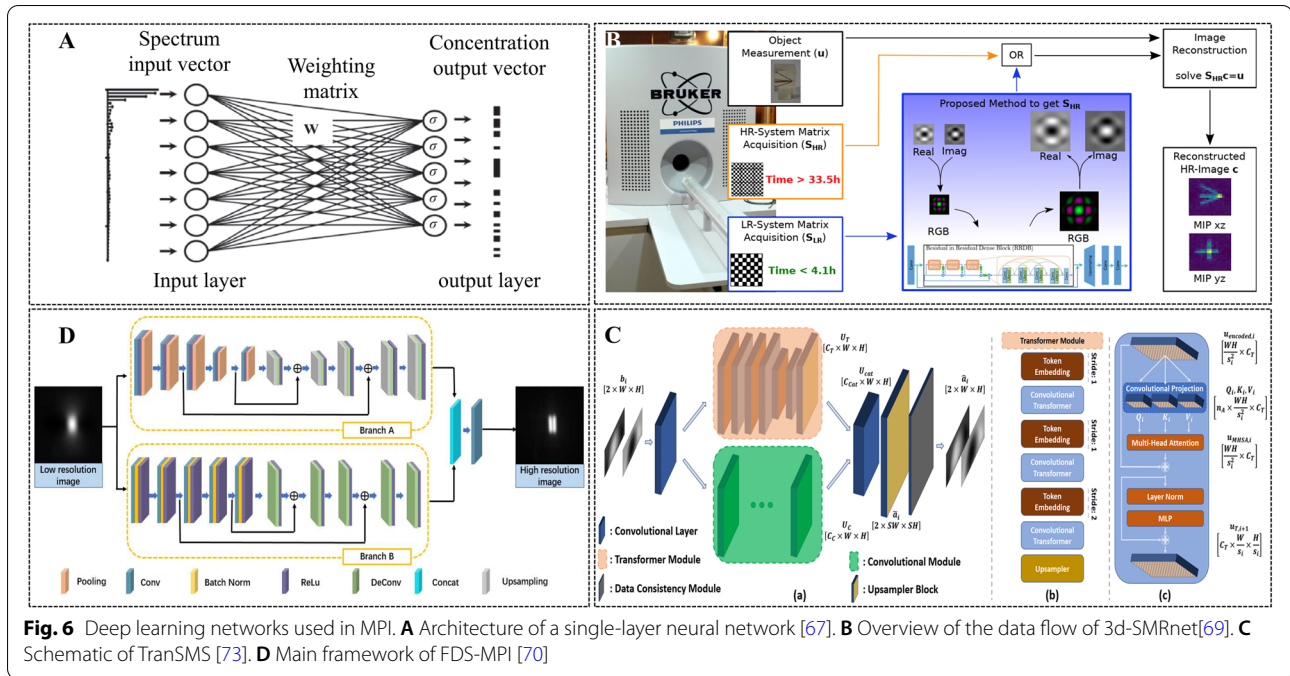
convolution kernel $q(t)$ ($q(t)$ denotes the relaxation process). Correspondingly, the nonadiabatic raw image is described as the temporal convolution of the adiabatic raw image and convolution kernel:

$$\hat{c}_D(\mathbf{r}) = \hat{c}_L(\mathbf{r}) * q(t) = (c(\mathbf{r}) * h(\mathbf{r})) * q(t) \qquad (19)$$

$\hat{c}_L$ denotes a raw image based on the Langevin model (ideal adiabatic conditions). The nonadiabatic X-space method based on the Debye relaxation model showed excellent consistency with the measured signals from the Berkeley MPI scanner [60].

The relaxation effect is caused by Néel and Brownian rotations of the SPIOs. In MPI, two rotations are coupled, and both rotations have their own relaxation times. However, the Debye model uses a relaxation time constant τ to represent all rotations, which cannot describe

the dynamic magnetization process or rotation mechanism in a complete and accurate manner [61]. Therefore, in recent years, many theoretical models have been developed to accurately describe the relaxation effects of SPIOs. Löwa et al. [62] proposed that the magnetization behavior of SPIOs should be quantified as a function of the excitation magnetic field, properties of SPIOs, and surrounding environment. At present, the Landau-Lifshitz-Gilbert model is the most comprehensive model for exploring the relaxation effect [63]. However, an obvious error is observed between the simulation and measurement results, and significant computational power is required to generate the solution [61]. The Fokker-Plank model explores the dependence of the relaxation time on the excitation field [64]. However, the solutions did not couple the Néel and Brownian rotations [65, 66]. The complex relaxation effect has an important influence on

Yin *et al. Visual Computing for Industry, Biomedicine, and Art*   (2022) 5:24

Page 9 of 13

Fig. 6 Deep learning networks used in MPI. **A** Architecture of a single-layer neural network [67]. **B** Overview of the data flow of 3d-SMRnet[69]. **C** Schematic of TranSMS [73]. **D** Main framework of FDS-MPI [70]

the reconstruction results of the x-space; therefore, conducting relevant research is crucial.

AI methods for MPI reconstruction

The development of deep learning technology based on AI has inspired new approaches to MPI reconstruction. Currently, AI is primarily applied in MPI reconstruction [67, 68], SM recovery [69], and image postprocessing [70].
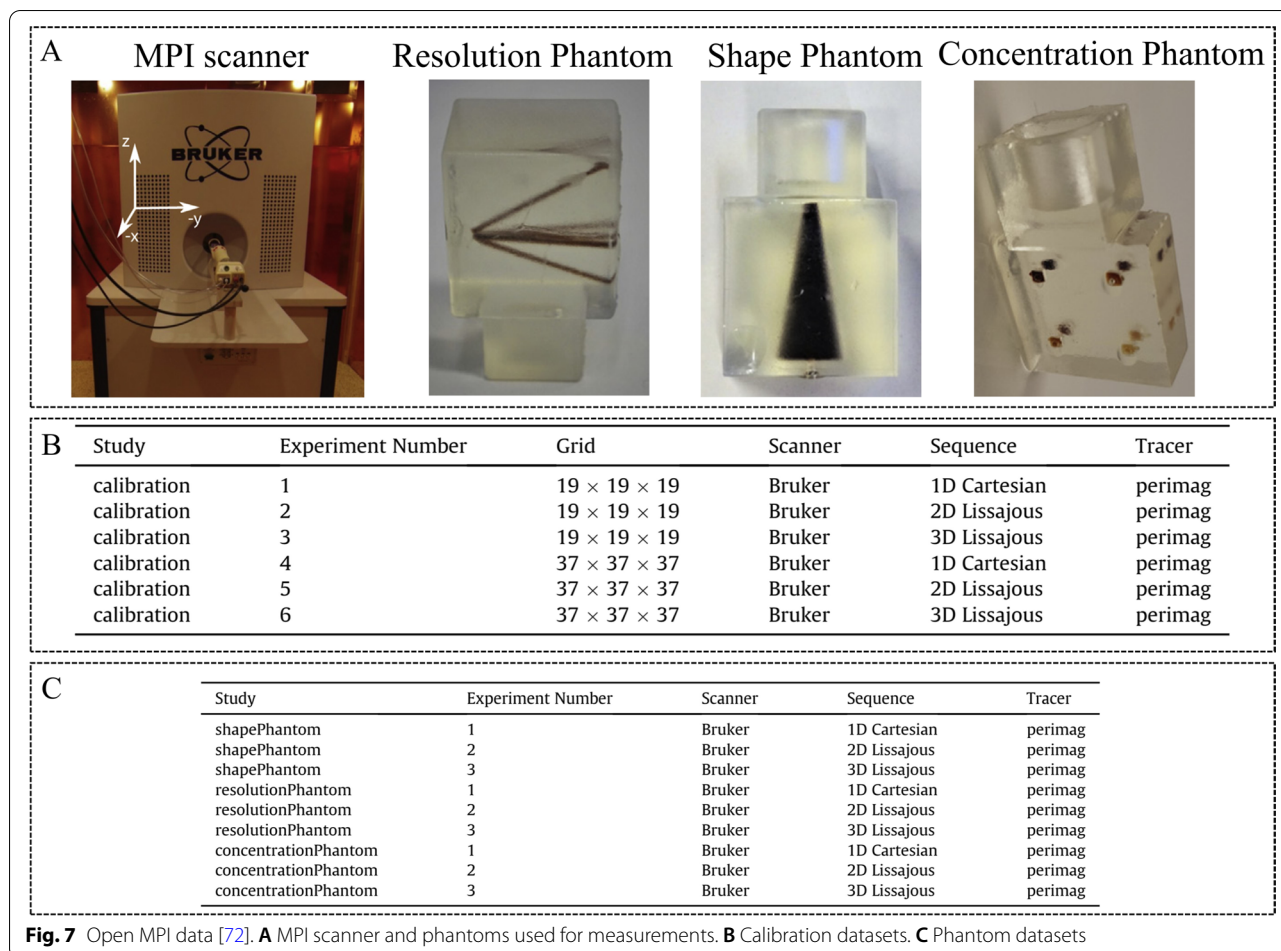
In 2017, Chae [67] proposed the reconstruction of MPI images using a single-layer fully connected network (Fig. 6 A). The input of the network is the voltage **u** in the frequency domain, and the output is the concentration distribution of the SPIOs **c**: $\mathbf{c} = \delta(\mathbf{W}\mathbf{u})$. δ is the activation function, and **W** represents the weighting matrix. The author constructed 30000 training datasets and 1000 test sets using 1D simulation. The test images were all reconstructed well by the trained network. The results showed that a neural network structure is expected to be a better tool for MPI image reconstruction because of its capacity to overcome the low incoherence of the inverse kernel through the classification property. Subsequently, Dittmer et al. [68] proposed a novel reconstruction framework based on a deep image prior (DIP). The basic idea of DIP is to use an untrained neural network that implicitly encodes a priori to perform a reliable reconstruction [71]. Compared with traditional variational and iterative regularization, it has significant advantages in terms of image quality [72].

The SM recovery problem was transformed into a super-resolution reconstruction problem for deep learning approaches. Baltruschat et al. [69] proposed the use of a 3D-SM recovery network (3D-SMRnet) to recover a 3D SM with an undersampling rate of less than 1.6% (Fig. 6 B). Their results showed that 3D-SMRnet is superior to the CS method in terms of SM recovery quality, reconstructed image quality, and performing time. In addition, Güngör et al. [73] proposed an SM super-resolution method based on transformer network architecture (TranSMS) (Fig. 6 C). Compared with state-of-the-art CS and deep learning baselines, TranSMS enables low-error SM recovery and high-quality MPI image reconstruction.

The advantage of deep learning technology in the field of image processing also inspired MPI image post-processing. Shang et al. [70] designed an end-to-end dual-sampling convolutional neural network to improve the spatial resolution of MPI (FDS-MPI) (Fig. 6 D). The results of the simulation, phantom, and in vivo experiments demonstrated the advantages of FDS-MPI in improving MPI image resolution. Deep learning technology plays an important role in signal and image processing. It has been applied to many medical modalities such as CT, MRI, and ultrasound. This will definitely shine in benefit MPI in the future.

Current open sources for MPI

Many countries, such as Germany, United States, Turkey, China, Japan, and South Korea, have conducted research on MPI. More importantly, many groups have created

Yin *et al. Visual Computing for Industry, Biomedicine, and Art* (2022) 5:24

Page 10 of 13

Fig. 7 Open MPI data [72]. **A** MPI scanner and phantoms used for measurements. **B** Calibration datasets. **C** Phantom datasets

Study	Experiment Number	Grid	Scanner	Sequence	Tracer
calibration	1	$19 \times 19 \times 19$	Bruker	1D Cartesian	perimag
calibration	2	$19 \times 19 \times 19$	Bruker	2D Lissajous	perimag
calibration	3	$19 \times 19 \times 19$	Bruker	3D Lissajous	perimag
calibration	4	$37 \times 37 \times 37$	Bruker	1D Cartesian	perimag
calibration	5	$37 \times 37 \times 37$	Bruker	2D Lissajous	perimag
calibration	6	$37 \times 37 \times 37$	Bruker	3D Lissajous	perimag

Study	Experiment Number	Scanner	Sequence	Tracer
shapePhantom	1	Bruker	1D Cartesian	perimag
shapePhantom	2	Bruker	2D Lissajous	perimag
shapePhantom	3	Bruker	3D Lissajous	perimag
resolutionPhantom	1	Bruker	1D Cartesian	perimag
resolutionPhantom	2	Bruker	2D Lissajous	perimag
resolutionPhantom	3	Bruker	3D Lissajous	perimag
concentrationPhantom	1	Bruker	1D Cartesian	perimag
concentrationPhantom	2	Bruker	2D Lissajous	perimag
concentrationPhantom	3	Bruker	3D Lissajous	perimag

open sources that allow novice groups to conduct MPI-related research as quickly as possible. In this section, we summarize widely used open sources.

Knopp et al. [72] published an article about Open MPI data in 2020, which provides experimental MPI and related data processing code for free. This benefits research groups without MPI systems to understand and analyze MPI experimental data. This dataset is stored in the MDF format, which is an open-document standard format. A pre-clinical MPI scanner (Bruker, Ettlingen) was used to acquire the MPI data, including three different phantoms and three different imaging sequences, as shown in Fig. 7. The CAD data of the phantoms are also provided. Furthermore, the Open MPI data also contain the SM based on the calibrations for different mesh densities (Fig. 7 B). Several groups have conducted research on image reconstruction, SM recovery, and other aspects based on Open MPI data [44, 68, 69].

In addition, Tian's team from the Chinese Academy of Sciences has conducted several MPI studies. They set up an MPI website (MPILabs, http://mpilab.net/en/simul ation) that exhibits relevant academic research, open-source experimental data, an algorithm framework, and a software platform. Notably, the software platform MPIRF developed in Python 3.8 integrates SM-based and x-space algorithms to realize MPI reconstruction from the voltage signal of SPIOs to the image [74].

Another public MPI site, open-Source MPI (https://os-mpi.github.io), is offered by Harvard Medical School and Massachusetts Institute of Technology. It publishes the MPI system design and basic components, as well as the associated auxiliary simulation algorithms. These MPI open sources have greatly promoted the development of MPI worldwide.

Conclusions and outlook

As a novel imaging technology, MPI has wide research and application prospects. This study primarily reviews MPI reconstruction techniques, the SM-based and x-space methods. For these, we provide a detailed review of the SM acquisition and reconstruction methods based on a regularization strategy. In addition, the x-space

Yin *et al. Visual Computing for Industry, Biomedicine, and Art*   (2022) 5:24

Page 11 of 13

reconstruction theory and corresponding improved algorithms based on the relaxation model were described. We also reviewed recent deep learning applications in MPI reconstruction and current open sources of MPI.

This review demonstrates the multifaceted nature of MPI. The main challenge for SM-based reconstruction in the future may involve obtaining the SM more quickly and accurately through modeling, measurement, or simulation; this requires a detailed understanding of the SM. In addition, the introduction of prior knowledge and deep learning technology to further improve the reconstruction performance of SM-based reconstruction remains a research focus. In terms of x-space methods, establishing a more accurate magnetization model to describe the relaxation or hysteresis effect is an important challenge to overcome. Furthermore, multi-contrast or multi-color reconstruction based on the specific physical properties of SPIOs, as well as sequence development and corresponding image reconstruction based on novel hardware design, are important challenges and interesting hot spots.

In the past 20 years, because of the tireless efforts of scientists worldwide, MPI has progressed considerably in equipment development, magnetic particle preparation, and reconstruction algorithm research, which have further promoted the application of MPI in clinical settings. We expect this review to provide references for MPI researchers and promote the development and future clinical applications of MPI.

Abbreviations
MPI: Magnetic particle imaging; SPIO: Superparamagnetic iron oxide particle; FFR: Field-free region; FOV: Field of view; CT: Computed tomography; MRI: Magnetic resonance imaging; PET: Positron emission tomography; SPECT: Single-photon emission computed tomography; FFL: Field-free line; FFP: Field-free point; 3D: Three-dimensional; SM: System matrix; CS: Compressed sensing; SNR: Signal-noise ratio; SVD: Singular value decomposition; LSI: Linear shift-invariant ; PVT: Paraventricular thalamic nucleus; 1D: One-dimensional; 2D: Two-dimensional; AI: Artificial intelligence; DIP: Deep image prior; 3D-SMRnet: 3D-SM recovery network.

Declarations

Ethics approval and consent to participate
Not applicable.

Consent for publication
All authors have approved the publication.

Competing interests
The authors declare that they have no competing interests.

Author details
[1]CAS Key Laboratory of Molecular Imaging, the State Key Laboratory of Management and Control for Complex Systems, Institute of Automation, Chinese Academy of Sciences, Beijing 100190, China. [2]Beijing Key Laboratory of Molecular Imaging, Beijing 100190, China. [3]University of Chinese Academy of Sciences, Beijing 100049, China. [4]Medical Imaging Center, the First Affiliated Hospital, Jinan University, Guangdong 510632, China. [5]Beijing Advanced Innovation Center for Big Data-Based Precision Medicine, School of Medicine, Beihang University, Beijing 100083, China.

References
1. Gleich B, Weizenecker J (2005) Tomographic imaging using the nonlinear response of magnetic particles. Nature 435(7046):1214-1217. https://doi.org/10.1038/nature03808
2. Weizenecker J, Gleich B, Rahmer J, Dahnke H, Borgert J (2009) Three-dimensional real-time in vivo magnetic particle imaging. Phys Med Biol 54(5):L1-L10. https://doi.org/10.1088/0031-9155/54/5/L01
3. Gräfe K, von Gladiss A, Bringout G, Ahlborg M, Buzug TM (2016) 2D images recorded with a single-sided magnetic particle imaging scanner. IEEE Trans Med Imaging 35(4):1056-1065. https://doi.org/10.1109/tmi.2015.2507187
4. Bulte JWM (2019) Superparamagnetic iron oxides as MPI tracers: a primer and review of early applications. Adv Drug Deliv Rev 138:293-301. https://doi.org/10.1016/j.addr.2018.12.007
5. Meribout M, Kalra M (2020) A portable system for two dimensional magnetic particle imaging. Measurement 152:107281. https://doi.org/10.1016/j.measurement.2019.107281
6. Le TA, Bui MP, Yoon J (2020) Design of a rabbit scale 3D magnetic particle imaging system with amplitude modulation. Int J Mag Part Imaging 6(2 Suppl 1):2009067. https://doi.org/10.18416/IJMPI.2020.2009067
7. Rahmer J, Weizenecker J, Gleich B, Borgert J (2009) Signal encoding in magnetic particle imaging: properties of the system function. BMC Med Imaging 9(1):4. https://doi.org/10.1186/1471-2342-9-4
8. Grüttner M, Knopp T, Franke J, Heidenreich M, Rahmer J, Halkola A et al (2013) On the formulation of the image reconstruction problem in magnetic particle imaging. Biomed Tech 58(6):583-591. https://doi.org/10.1515/bmt-2012-0063
9. Venneti S, Dunphy MP, Zhang HW, Pitter KL, Zanzonico P, Campos C et al (2015) Glutamine-based PET imaging facilitates enhanced metabolic evaluation of gliomas in vivo. Sci Transl Med 7(274):274ra17. https://doi.org/10.1126/scitranslmed.aaa1009
10. Yin L, Wang K, Tong T, An Y, Meng H, Yang X et al (2020) Improved block sparse Bayesian learning method using K-nearest neighbor strategy for accurate tumor morphology reconstruction in bioluminescence tomography. IEEE Trans Biomed Eng 67(7):2023-2032. https://doi.org/10.1109/TBME.2019.2953732
11. Rowe SP, Pomper MG (2022) Molecular imaging in oncology: current impact and future directions. CA: Cancer J Clin 72(4):333-352. https://doi.org/10.3322/caac.21713

12. Wu LC, Zhang Y, Steinberg G, Qu H, Huang S, Cheng M et al (2019) A review of magnetic particle imaging and perspectives on neuroimaging. AJNR Am J Neuroradiol 40(2):206-212. https://doi.org/10.3174/ajnr.A5896

13. Tay ZW, Chandrasekharan P, Chiu-Lam A, Hensley DW, Dhavalikar R, Zhou XY et al (2018) Magnetic particle imaging-guided heating in vivo using gradient fields for arbitrary localization of magnetic hyperthermia therapy. ACS Nano 12(4):3699-3713. https://doi.org/10.1021/acsnano.8b00893

14. Yu EY, Chandrasekharan P, Berzon R, Tay ZW, Zhou XY, Khandhar AP et al (2017) Magnetic particle imaging for highly sensitive, quantitative, and safe in vivo gut bleed detection in a murine model. ACS Nano 11(12):12067-12076. https://doi.org/10.1021/acsnano.7b04844

15. Song GS, Chen M, Zhang YR, Cui LY, Qu HB, Zheng XC et al (2018) Janus iron oxides @ semiconducting polymer nanoparticle tracer for cell tracking by magnetic particle imaging. Nano Lett 18(1):182-189. https://doi.org/10.1021/acs.nanolett.7b03829

16. Song GS, Zheng XC, Wang YJ, Xia X, Chu S, Rao JH (2019) A magneto-optical nanoplatform for multimodality imaging of tumors in mice. ACS Nano 13(7):7750-7758. https://doi.org/10.1021/acsnano.9b01436

17. Tomitaka A, Arami H, Gandhi S, Krishnan KM (2015) Lactoferrin conjugated iron oxide nanoparticles for targeting brain glioma cells in magnetic particle imaging. Nanoscale 7(40):16890-16898. https://doi.org/10.1039/c5nr02831k

18. Parkins KM, Melo KP, Chen YX, Ronald JA, Foster PJ (2021) Visualizing tumour self-homing with magnetic particle imaging. Nanoscale 13(12):6016-6023. https://doi.org/10.1039/d0nr07983a

19. Orendorff R, Peck AJ, Zheng B, Shirazi SN, Ferguson RM, Khandhar AP et al (2017) First in vivo traumatic brain injury imaging via magnetic particle imaging. Phys Med Biol 62(9):3501. https://doi.org/10.1088/1361-6560/aa52ad

20. Szwargulski P, Wilmes M, Javidi E, Thieben F, Graeser M, Koch M et al (2020) Monitoring intracranial cerebral hemorrhage using multicontrast real-time magnetic particle imaging. ACS Nano 14(10):13913-13923. https://doi.org/10.1021/acsnano.0c06326

21. You HJ, Shang WT, Min XD, Weinreb J, Li QB, Leapman M et al (2020) Sight and switch off: nerve density visualization for interventions targeting nerves in prostate cancer. Sci Adv 6(6):6040

22. Gleich B, Weizenecker J, Borgert J (2008) Experimental results on fast 2D-encoded magnetic particle imaging. Phys Med Biol 53(6):N81-N84. https://doi.org/10.1088/0031-9155/53/6/N01

23. Weizenecker J, Gleich B, Borgert J (2008) Magnetic particle imaging using a field free line. J Phys D: Appl Phys 41(10):105009. https://doi.org/10.1088/0022-3727/41/10/105009

24. Top CB, Güngör A, Ilbey S, Güven HE (2019) Trajectory analysis for field free line magnetic particle imaging. Med Phys 46(4):1592-1607. https://doi.org/10.1002/mp.13411

25. Knopp T, Erbe M, Biederer S, Sattel TF, Buzug TM (2010) Efficient generation of a magnetic field-free line. Med Phys 37(7):3538-3540. https://doi.org/10.1118/1.3447726

26. Bente K, Weber M, Graeser M, Sattel TF, Erbe M, Buzug TM (2014) Electronic field free line rotation and relaxation deconvolution in magnetic particle imaging. IEEE Trans Med Imaging 34(2):644-651. https://doi.org/10.1109/TMI.2014.2364891

27. Sattel TF, Knopp T, Biederer S, Gleich B, Weizenecker J, Borgert J et al (2009) Single-sided device for magnetic particle imaging. J Phys D: Appl Phys 42(2):022001. https://doi.org/10.1088/0022-3727/42/2/022001

28. Vogel P, Rückert MA, Klauer P, Kullmann WH, Jakob PM, Behr VC (2015) Superspeed traveling wave magnetic particle imaging. IEEE Trans Magn 51(2):6501603. https://doi.org/10.1109/TMAG.2014.2322897

29. Franke J, Heinen U, Lehr H, Weber A, Jaspard F, Ruhm W et al (2016) System characterization of a highly integrated preclinical hybrid mpi-mri scanner. IEEE Trans Med Imaging 35(9):1993-2004. https://doi.org/10.1109/TMI.2016.2542041

30. Gräser M, Thieben F, Szwargulski P, Werner F, Gdaniec N, Boberg M et al (2019) Human-sized magnetic particle imaging for brain applications. Nat Commun 10(1):1936. https://doi.org/10.1038/s41467-019-09704-x

31. Top CB, Güngör A (2020) Tomographic field free line magnetic particle imaging with an open-sided scanner configuration. IEEE Trans Med Imaging 39(12):4164-4173. https://doi.org/10.1109/TMI.2020.3014197

32. Mason EE, Mattingly E, Herb K, Śliwiak M, Franconi S, Cooley CZ et al (2021) Concept for using magnetic particle imaging for intraoperative margin analysis in breast-conserving surgery. Sci Rep 11(1):13456. https://doi.org/10.1038/s41598-021-92644-8

33. Ilbey S, Top CB, Güngör A, Çukur T, Saritas EU, Güven HE (2017) Comparison of system-matrix-based and projection-based reconstructions for field free line magnetic particle imaging. Int J Mag Part Imag 3(1):1703022. https://doi.org/10.18416/ijmpi.2017.1703022

34. Kaethner C, Erb W, Ahlborg M, Szwargulski P, Knopp T, Buzug TM (2016) Non-equispaced system matrix acquisition for magnetic particle imaging based on lissajous node points. IEEE Trans Med Imaging 35(11):2476-2485. https://doi.org/10.1109/TMI.2016.2580458

35. Panagiotopoulos N, Duschka RL, Ahlborg M, Bringout G, Debbeler C, Graeser M et al (2015) Magnetic particle imaging: current developments and future directions. Int J Nanomed 10(1):3097-3114. https://doi.org/10.2147/IJN.S70488

36. Rahmer J, Weizenecker J, Gleich B, Borgert J (2012) Analysis of a 3-D system function measured for magnetic particle imaging. IEEE Trans Med Imaging 31(6):1289-1299. https://doi.org/10.1109/TMI.2012.2188639

37. Knopp T, Weber A (2013) Sparse reconstruction of the magnetic particle imaging system matrix. IEEE Trans Med Imaging 32(8):1473-1480. https://doi.org/10.1109/TMI.2013.2258029

38. Knopp T, Sattel TF, Biederer S, Rahmer J, Weizenecker J, Gleich B et al (2010) Model-based reconstruction for magnetic particle imaging. IEEE Trans Medical Imaging 29(1):12-18. https://doi.org/10.1109/TMI.2009.2021612

39. Goodwill PW, Conolly SM (2010) The X-space formulation of the magnetic particle imaging process: 1-D signal, resolution, bandwidth, SNR, SAR, and magnetostimulation. IEEE Trans Med Imaging 29(11):1851-1859. https://doi.org/10.1109/TMI.2010.2052284

40. Goodwill PW, Saritas EU, Croft LR, Kim TN, Krishnan KM, Schaffer DV et al (2012) X-space MPI: magnetic nanoparticles for safe medical imaging. Adv Mat 24(28):3870-3877. https://doi.org/10.1002/adma.201200221

41. Ozaslan AA, Alacaoglu A, Demirel OB, Çukur T, Saritas EU (2019) Fully automated gridding reconstruction for non-cartesian x-space magnetic particle imaging. Phys Med Biol 64(16):165018. https://doi.org/10.1088/1361-6560/ab3525

42. Kurt S, Muslu Y, Saritas EU (2020) Partial FOV center imaging (PCI): a robust X-space image reconstruction for magnetic particle imaging. IEEE Trans Med Imaging 39(11):3441-3450. https://doi.org/10.1109/TMI.2020.2995410

43. Szwargulski P, Möddel M, Gdaniec N, Knopp T (2019) Efficient joint image reconstruction of multi-patch data reusing a single system matrix in magnetic particle imaging. IEEE Trans Med Imaging 38(4):932-944. https://doi.org/10.1109/TMI.2018.2875829

44. Grosser M, Möddel M, Knopp T (2020) Using low-rank tensors for the recovery of MPI system matrices. IEEE Trans Comput Imaging 6:1389-1402. https://doi.org/10.1109/TCI.2020.3024078

45. Weber A, Knopp T (2015) Reconstruction of the magnetic particle imaging system matrix using symmetries and compressed sensing. Adv Math Phys 2015:460496. https://doi.org/10.1155/2015/460496

46. Ilbey S, Top CB, Güngör A, Çukur T, Saritas EU, Güven HE (2019) Fast system calibration with coded calibration scenes for magnetic particle imaging. IEEE Trans Med Imaging 38(9):2070-2080. https://doi.org/10.1109/TMI.2019.2896290

47. Knopp T, Biederer S, Sattel TF, Rahmer J, Weizenecker J, Gleich B et al (2010) 2D model-based reconstruction for magnetic particle imaging. Med Phys 37(2):485-491. https://doi.org/10.1118/1.3271258

48. Takagi T, Tsuchiya H, Hatsuda T, Ishihara Y (2016) Image reconstruction method using orthonormal basis by singular value decomposition for magnetic particle imaging. Trans Japanese Soc Med Biol Eng 53(5):276-282. https://doi.org/10.11239/jsmbe.53.276

49. Kluth T, Jin BT (2019) Enhanced reconstruction in magnetic particle imaging by whitening and randomized SVD approximation. Phys Med Biol 64(12):125026. https://doi.org/10.1088/1361-6560/ab1a4f

50. Knopp T, Rahmer J, Sattel TF, Biederer S, Weizenecker J, Gleich B et al (2010) Weighted iterative reconstruction for magnetic particle imaging. Phys Med Biol 55(6):1577-1589. https://doi.org/10.1088/0031-9155/55/6/003

51. Knopp T, Hofmann M (2016) Online reconstruction of 3D magnetic particle imaging data. Phys Med Biol 61(11):N257-N267. https://doi.org/10.1088/0031-9155/61/11/N257

52. Hsieh SS, Hoffman JM, Noo F (2019) Accelerating iterative coordinate descent using a stored system matrix. Med Phys 46(12):e801-e809. https://doi.org/10.1002/mp.13543
53. Chen XJ, Jiang ZQ, Han X, Wang XL, Tang XY (2021) The reconstruction of magnetic particle imaging: current approaches based on the system matrix. Diagnostics 11(5):773. https://doi.org/10.3390/diagnostics11050773
54. Schmiester L, Möddel M, Erb W, Knopp T (2017) Direct image reconstruction of lissajous-type magnetic particle imaging data using chebyshev-based matrix compression. IEEE Trans Comput Imaging 3(4):671-681. https://doi.org/10.1109/TCI.2017.2706058
55. Storath M, Brandt C, Hofmann M, Knopp T, Salamon J, Weber A et al (2017) Edge preserving and noise reducing reconstruction for magnetic particle imaging. IEEE Trans Med Imaging 36(1):74-85. https://doi.org/10.1109/TMI.2016.2593954
56. Goodwill PW, Conolly SM (2011) Multidimensional X-space magnetic particle imaging. IEEE Trans Med Imaging 30(9):1581-1590. https://doi.org/10.1109/TMI.2011.2125982
57. Goodwill PW, Konkle JJ, Zheng B, Saritas EU, Conolly SM (2012) Projection X-space magnetic particle imaging. IEEE Trans Med Imaging 31(5):1076-1085. https://doi.org/10.1109/TMI.2012.2185247
58. Ferguson RM, Minard KR, Khandhar AP, Krishnan KM (2011) Optimizing magnetite nanoparticles for mass sensitivity in magnetic particle imaging. Med Phys 38(3):1619-1626. https://doi.org/10.1118/1.3554646
59. Ferguson RM, Minard KR, Krishnan KM (2009) Optimization of nanoparticle core size for magnetic particle imaging. J Magn Magn Mater 321(10):1548-1551. https://doi.org/10.1016/j.jmmm.2009.02.083
60. Croft LR, Goodwill PW, Conolly SM (2012) Relaxation in X-space magnetic particle imaging. IEEE Trans Med Imaging 31(12):2335-2342. https://doi.org/10.1109/TMI.2012.2217979
61. Shasha C, Krishnan KM (2021) Nonequilibrium dynamics of magnetic nanoparticles with applications in biomedicine. Adv Mater 33(23):1904131. https://doi.org/10.1002/adma.201904131
62. Löwa N, Seidel M, Radon P, Wiekhorst F (2017) Magnetic nanoparticles in different biological environments analyzed by magnetic particle spectroscopy. J Magn Magn Mater 427:133-138. https://doi.org/10.1016/j.jmmm.2016.10.096
63. Kluth T (2018) Mathematical models for magnetic particle imaging. Inverse Probl 34(8):083001. https://doi.org/10.1088/1361-6420/aac535
64. Albers H, Kluth T, Knopp T (2022) Simulating magnetization dynamics of large ensembles of single domain nanoparticles: numerical study of brown/néel dynamics and parameter identification problems in magnetic particle imaging. J Magn Magn Mater 541:168508. https://doi.org/10.1016/j.jmmm.2021.168508
65. Deissler RJ, Wu Y, Martens MA (2014) Dependence of Brownian and Néel relaxation times on magnetic field strength. Med Phys 41(1):012301. https://doi.org/10.1118/1.4837216
66. Deissler RJ, Martens MA (2015) Dependence of the magnetization response on the driving field amplitude for magnetic particle imaging and spectroscopy. IEEE Trans Magn 51(2):6500904. https://doi.org/10.1109/TMAG.2014.2322579
67. Chae BG (2017) Neural network image reconstruction for magnetic particle imaging. ETRI J 39(6):841-850. https://doi.org/10.4218/etrij.2017-0094
68. Dittmer S, Kluth T, Henriksen MTR, Maass P (2020) Deep image prior for 3D magnetic particle imaging: a quantitative comparison of regularization techniques on open MPI dataset. arXiv preprint arXiv:2007.01593. https://doi.org/10.48550/arXiv.2007.01593
69. Baltruschat IM, Szwargulski P, Griese F, Grosser M, Werner R, Knopp T (2020) 3D-smrnet: achieving a new quality of MPI system matrix recovery by deep learning. In: Martel AL, Abolmaesumi P, Stoyanov D, Mateus D, Zuluaga MA, Zhou SK et al (eds) 23rd international conference on medical image computing and computer-assisted intervention, Lima, Peru, October 2020. Lecture notes in computer science book series, vol 12262. Springer, Lima, pp. 74-82
70. Shang YX, Liu J, Zhang LW, Wu XJ, Zhang P, Yin L et al (2022) Deep learning for improving the spatial resolution of magnetic particle imaging. Phys Med Biol 67(12):125012. https://doi.org/10.1088/1361-6560/ac6e24
71. Ulyanov D, Vedaldi A, Lempitsky V (2018) Deep image prior. Paper presented at the IEEE conference on computer vision and pattern recognition, IEEE, Salt Lake City, 18-23 June 2018
72. Knopp T, Szwargulski P, Griese F, Gräser M (2020) OpenMPIData: an initiative for freely accessible magnetic particle imaging data. Data Brief 28:104971. https://doi.org/10.1016/j.dib.2019.104971
73. Güngör A, Askin B, Soydan DA, Saritas EU, Top CB, Çukur T (2021) TranSMS: transformers for super-resolution calibration in magnetic particle imaging. arXiv preprint arXiv:2111.02163. https://doi.org/10.48550/arXiv.2111.02163
74. Shen YS, Hu CE, Zhang P, Tian J, Hui H (2022) A novel software framework for magnetic particle imaging reconstruction. Int J Imaging Syst Technol 32(4):1119-1132. https://doi.org/10.1002/ima.22707

Publisher's Note